INTERFACIAL AREA TRANSPORT IN TWO-PHASE FLOWS IN A SCALED 8X8 ROD BUNDLE GEOMETRY AT ELEVATED PRESSURES

X. Yang[1], J. P. Schlegel[1], S. Paranjape[1], Y. Liu[1], S.W. Chen[1], T. Hibiki[1] and M. Ishii[1]
[1] School of Nuclear Engineering, Purdue University
400 Central Drive, West Lafayette, IN 47907, USA
yang139@purdue.edu, jschlege@purdue.edu, paranjap@purdue.edu, liu130@purdue.edu, swchen@purdue.edu, hibiki@purdue.edu, ishii@purdue.edu

Abstract

To improve the prediction accuracy and robustness of the next-generation thermal-hydraulics system analysis code, analytical and experimental research has been undertaken to develop the Interfacial Area Transport Equation (IATE) in a scaled 8x8 rod bundle geometry at elevated pressure conditions. The experiments performed include local measurements of void fraction, interfacial area concentration, and gas velocity at several axial locations using the innovative four-sensor conductivity probe. The test conditions cover a wide range of flow regimes from bubbly, cap-bubbly, cap-turbulent to churn-turbulent at 100 kPa and 300 kPa pressure conditions and the obtained data indicates some spacer effects on the flow parameters. The bubble groups are classified into two groups (Group-1: spherical and distorted bubbles, Group-2: cap and churn turbulent bubbles) based on the bubble transport characteristics. The area-averaged interfacial area transport data have been compared to the prediction by the one-dimensional two-group IATE with mechanistically modeled IAC source and sink terms. The one-group IATE is able to predict the bubbly-flow interfacial area within ±15% error under two pressure conditions. The two-group IATE performance is also very promising in the cap-bubbly flow and churn-turbulent flow regimes, with average error of about ±20%.

Keywords: Interfacial Area Transport Equation, Rod Bundle, Sub-Channel, Two-Fluid Model,

1. Introduction

The next generation of nuclear reactor designs will have their safety characteristics and performance evaluated using advanced thermal-hydraulics analysis codes. Currently, these codes utilize static, flow regime dependent correlations to predict the interfacial geometry, which is important in the prediction of interfacial transfer of mass, momentum, and energy. This approach results in two levels of error, the first being the prediction of flow regime based on static flow regime maps and the second being the uncertainty in the constitutive models for interfacial area concentration. Additionally, these correlations are developed for static, fully developed systems making them unsuitable for transients or dynamic systems. For this reason an effort has been initiated to develop the Interfacial Area Transport Equation (IATE) for the prediction of interfacial area concentration in dynamic systems. In addition to reducing numerical bifurcation and improving accuracy for dynamic systems, the IATE formulation is consistent for three-dimensional and one-dimensional systems, meaning that it can easily be used in CFD simulations in addition to one-dimensional calculations.

Previous research has developed the necessary foundation for the IATE and experimental techniques for the measurement of interfacial area concentration and other important bubble characteristics. An extensive review of the available literature regarding data and modeling efforts has been performed[1-3] and has found that very little data is available on interfacial area concentration or interfacial area transport for scaled bundle systems such as those simulating actual BWR assemblies[4]. Thus analytical and experimental research has been performed to develop the accurate IATE models for use in complex geometries. An experiment has been performed to develop an extensive database of local flow parameters in a scaled 8x8 rod bundle geometry to model and benchmark the IATE.

2. Two-Group IATE

The IATE was rigorously formulated based on the Boltzmann transport equation in order to model the interfacial geometry of two-phase flows[3]. In order to account for the differences between the transport characteristics of smaller spherical or distorted bubbles (Group-1 bubbles) and larger cap or churn-turbulent bubbles (Group-2), the one-dimensional two-group IATE for adiabatic systems has been proposed as[3]

$$\frac{\partial \langle a_{i1} \rangle}{\partial t} + \frac{\partial}{\partial z} \langle a_{i1} \rangle \langle\langle v_{i1} \rangle\rangle = \left(\frac{2}{3} - C \left(D_{c1}^{*} \right)^{2} \right) \frac{\langle a_{i1} \rangle}{\langle \alpha_1 \rangle} \frac{\partial}{\partial z} \langle \alpha_1 \rangle \langle\langle v_{g1} \rangle\rangle + \sum_j \langle \phi_{j1} \rangle \quad (1)$$

$$\frac{\partial \langle a_{i2} \rangle}{\partial t} + \frac{\partial}{\partial z} \langle a_{i2} \rangle \langle\langle v_{i2} \rangle\rangle = \frac{2 \langle a_{i2} \rangle}{3 \langle \alpha_2 \rangle} \frac{\partial}{\partial z} \langle \alpha_2 \rangle \langle\langle v_{g2} \rangle\rangle + C \left(D_{c1}^{*} \right)^{2} \frac{\langle a_{i1} \rangle}{\langle \alpha_1 \rangle} \frac{\partial}{\partial z} \langle \alpha_1 \rangle \langle\langle v_{g1} \rangle\rangle + \sum_j \langle \phi_{j2} \rangle \quad (2)$$

where α_k, a_{ik}, v_{ik} and v_{gk} are the void fraction, interfacial area concentration, interfacial velocity, and gas velocity for group k (k =1 or 2) bubbles, respectively. The source and sink term for the interfacial area concentration due to bubble interactions for group-k bubbles is $\phi_{j,k}$. C is a coefficient related to the inter-group transport due to bubble expansion or compression at the group boundary. The boundary between the bubble groups is determined as [3]

$$D_b = 1.7 G^{1/3} \sqrt{\frac{\sigma}{g \Delta \rho}}, \quad (3)$$

where G is the gap size for confined geometries. This two-group model allows accurate prediction of interfacial area concentration in the slug or cap-turbulent regime, as these flow regimes exhibit two major bubble groups.

The source and sink mechanisms for interfacial area concentration change due to bubble interactions are shown in Fig. 1. In the figure, circular bubbles represent those in Group 1 while hemispherical bubbles represent those in Group 2. These source and sink terms are also noted in Table 1, in which "(1) + (1) = (2)" represents two Group 1 bubbles coalesce and form a Group 2 bubble, etc. Models were developed for these source and sink mechanisms for flow in confined rectangular channels with width W and gap size G. These models are

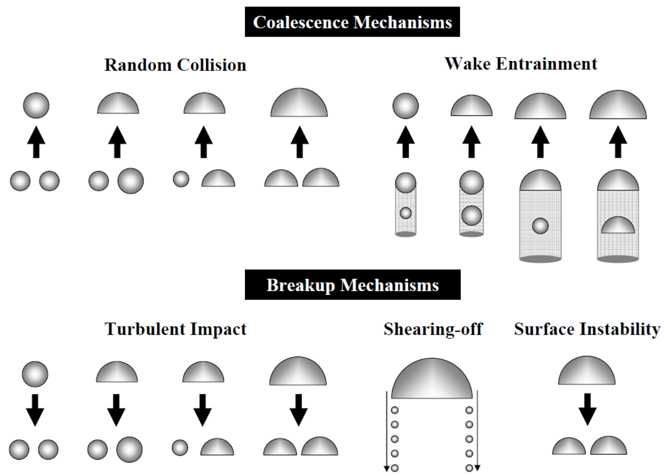

Figure 1 Bubble Interaction Mechanisms

briefly summarized in the table, for details on the development of the model the reader is referred to Ishii and Hibiki [3]. This confined channel is reasonably similar in geometry to a rod bundle and therefore serves as a convenient starting point for the development of models for a rod bundle.

In order to account for the geometry variations between rod bundles and confined rectangular channels, the following modification is proposed. First, the channel width, W, will be replaced by the casing dimension of the bundle representing the longest length scale for the flow. The gap size, G, will be replaced with the parameter h, which is defined as

$$h = k_s\left(P/\sqrt{2} - D_r\right). \tag{6}$$

where k_s is a constant whose value is approximately 0.8. The formula for h is derived from the maximum size of a cap bubble in a subchannel and represents the maximum size a group 2 bubble can reach before being distorted by the presence of the fuel rods. The constant k_s is determined from experimental data. This accounts for the second significant length scale affecting flows in rod bundles.

3. Experimental Facility

The experimental facility for these experiments is shown in Fig. 2. Liquid flow is measured using an electromagnetic flow meter with ±1% uncertainty, while gas flow is measured using rotameters or Venturi flow meters with ±3% uncertainty. Pressure at each measurement location is measured using differential pressure transducers with uncertainty of ±0.25% of the full measurement range. The test section is composed of a stainless steel outer casing with square cross section and side length of 140 mm. Inside the casing are 64 stainless steel rods with diameter of 10.3 mm and pitch of 16.7 mm. These values have been carefully determined by a detailed scaling analysis based on actual BWR bundle specifications. Spacer grids, which function as they do in actual reactor systems to maintain the spacing between the rods, are located in the test section at axial locations of z/D = 21, 42, 63, 83, 104, 123 and 143, where D = 2.14 cm is the subchannel hydraulic diameter and z is the distance from the test section inlet. Measurements are obtained at four locations with z/D = 5, 77, 85 and 137. The arrangement of the rods and spacer grids can be observed in the image on the right side of the figure, which shows the bottom half of the test section. The measurement locations at z/D = 77 and 85 are just before and just after a spacer grid, allowing evaluation of the effect of the spacer grid on the two-phase flow pattern.

Table 1 Significant Bubble Interaction Models

Notation	Model	Description
$RC^{(1)}$	$\phi_{RC}^{(1)} = -0.17\ C_{RC}^{(1)} \frac{\varepsilon^{1/3}\alpha_1^{1/3}a_{i1}^{5/3}}{\alpha_{1,\max}^{1/3}\left(\alpha_{1,\max}^{1/3}-\alpha_1^{1/3}\right)}\left[1-\exp\left(-C_{RC1}\frac{\alpha_{1,\max}^{1/3}\alpha_1^{1/3}}{\alpha_{1,\max}^{1/3}-\alpha_1^{1/3}}\right)\right]$	Random Collision, (1)+(1)=(1)
$RC^{(11,2)}$	$\phi_{RC,2}^{(11,2)} = 0.68\ C_{RC}^{(1)}\varepsilon^{1/3}\frac{\alpha_1^2 a_{i1}^{2/3}}{\alpha_{1,\max}^{2/3}G}\left[1-\exp\left(-C_{RC1}\frac{\alpha_{1,max}^{1/3}\alpha_1^{1/3}}{\alpha_{1,max}^{1/3}-\alpha_1^{1/3}}\right)\right]\left[1+0.7G^{7/6}\left(\frac{a_{i1}}{\alpha_1}\right)^{1/2}\left(\frac{\sigma}{g\Delta\rho}\right)^{-1/3}\right]\left(1-\frac{2}{3}D_{c1}^*\right)$	Random Collision, (1)+(1)=(2)
$RC^{(12,2)}$	$\phi_{RC,1}^{(12,2)} = -4.85\ C_{RC}^{(12,2)}\varepsilon^{1/3}\frac{a_{i1}\alpha_1^{2/3}\alpha_2^2}{R_{m2}^{2/3}}\left[1-\exp\left(-C_{RC1}\frac{\alpha_{1,\max}^{1/3}\alpha_1^{1/3}}{\left(\alpha_{1,\max}^{1/3}-\alpha_1^{1/3}\right)}\right)\right]$ $\phi_{RC,2}^{(12,2)} = 13.6\ C_{RC}^{(12,2)}\varepsilon^{1/3}\frac{\alpha_1^{5/3}\alpha_2^2}{R_{m2}^{2/3}G}\left(1+\frac{10.3G}{R_{m2}}\right)\left[1-exp\left(-\frac{C_{RC1}\alpha_{1,max}^{1/3}\alpha_1^{1/3}}{\left(\alpha_{1,max}^{1/3}-\alpha_1^{1/3}\right)}\right)\right]$	Random Collision, (1)+(2)=(2)
$RC^{(2)}$	$\phi_{RC}^{(2)} = -13.6C_{RC}^{(2)}\frac{\alpha_2^2\varepsilon^{1/3}}{W^2G}R_{m2}{}^{4/3}\left(1-2.0R_c^{*2}+\frac{9.0G}{R_{m2}}\right)\left[1-exp\left(-C_{RC2}\alpha_2^{1/2}\right)\right]$	Random Collision, (2)+(2)=(2)
$WE^{(1)}$	$\phi_{WE}^{(1)} = -0.27\ C_{WE}^{(1)}\ u_{r1}C_{D1}{}^{1/3}a_{i1}^2$	Wake Entrainment, (1)+(1)=(1)
$WE^{(11,2)}$	$\phi_{WE,2}^{(11,2)} = 1.08\ C_{WE}^{(11,2)}u_{r1}C_{D1}{}^{1/3}\frac{\alpha_1 a_{i1}}{G}\left(1-\frac{2}{3}D_{c1}^*\right)\left[1+0.7G^{7/6}\left(\frac{a_{i1}}{\alpha_1}\right)^{1/2}\left(\frac{\sigma}{g\Delta\rho}\right)^{-1/3}\right]$	Wake Entrainment, (1)+(1)=(2)
$WE^{(12,2)}$	$\phi_{WE,1}^{(12,2)} = -4.35\ C_{WE}^{(12,2)}\sqrt{gC_{D2}G}\frac{a_{i1}\alpha_2}{R_{m2}}$ $\phi_{WE,2}^{(12,2)} = 26.1\ C_{WE}^{(12,2)}\alpha_1\alpha_2\sqrt{\frac{gC_{D2}}{G}}\frac{1}{R_{m2}}\left(1+4.31\frac{G}{R_{m2}}\right)$	Wake Entrainment, (1)+(2)=(2)
$WE^{(2)}$	$\phi_{WE}^{(2)} = -15.9\ C_{WE}^{(2)}\ \frac{\alpha_2^2}{R_{m2}^2}\sqrt{C_D gG}\left(1+0.51R_c^*\right).$	Wake Entrainment, (2)+(2)=(2)
$TI^{(1)}$	$\phi_{TI}^{(1)} = 0.12C_{TI}^{(1)}\varepsilon^{1/3}(1-\alpha)\frac{a_{i1}^{5/3}}{\alpha_1^{2/3}}\exp\left(-\frac{We_{c,TI1}}{We_1}\right)\sqrt{1-\frac{We_{c,TI1}}{We_1}}$	Turbulent Impact, (1)=(1)+(1)
$TI^{(2,11)}$	$\phi_{TI,1}^{(2,1)} = 2.71\ C_{TI}^{(2)}\varepsilon^{1/3}G^{2/3}\alpha_2(1-\alpha)\frac{R_c^{*5/3}\left(1-R_c^{*5/3}\right)}{R_{m2}{}^{7/3}}\exp\left(-\frac{We_{c,TI2}}{We_2}\right)\sqrt{1-\frac{We_{c,TI2}}{We_2}},$	Turbulent Impact, (2)=(1)+(1)
$TI^{(2)}$	$\phi_{TI,2}^{(2)} = 1.4\ C_{TI}^{(2)}\alpha_2\frac{\varepsilon^{1/3}G}{R_{m2}^{8/3}}(1-\alpha)\left(1-2R_c^*\right)\exp\left(-\frac{We_{c,TI2}}{We_2}\right)\sqrt{1-\frac{We_{c,TI2}}{We_2}}$	Turbulent Impact, (2)=(2)+(2)
SO	$\phi_{SO,1}^{(2,12)} = 64.51\ C_{SO}C_d{}^2\frac{\alpha_2 v_{rb}}{GR_{m2}}\left(1-\left(\frac{We_{c,SO}}{We_{m2}}\right)^3\right)$ $\phi_{SO,2}^{(2,12)} = -21.50\ C_{SO}C_d{}^3\left(\frac{\sigma}{\rho_f}\right)^{3/5}\frac{\alpha_2 v_{rb}{}^{1-n}}{G^{8/5}R_{m2}}\left[1-\left(\frac{We_{c,SO}}{We_{m2}}\right)^3+\frac{3.24G}{R_{m2}}\left(1-\left(\frac{We_{c,SO}}{We_{m2}}\right)^2\right)\right],$	Shearing off, (2)=(2)+N(1)
SI	$\phi_{SI}^{(2)} = 1.25\ \alpha_2^2\left(\frac{\sigma}{g\Delta\rho}\right)^{-1}\left\{C_{RC}^{(2)}\frac{\varepsilon^{1/3}}{W^2}\left(\frac{\sigma}{g\Delta\rho}\right)^{7/6}\left[1-\exp\left(-C_{RC2}\alpha_2^{1/2}\right)\right]+2.3\bullet10^{-4}\ C_{WE}^{(2)}\sqrt{C_D gG}\right\}$	Surface Instability, (2)=(2)+(2)
EXP	$\phi_{EXP}^{(1)} = \frac{2}{3}\frac{\langle a_{i1}\rangle}{\langle\alpha_1\rangle}\frac{\partial}{\partial z}\langle\alpha_1\rangle\langle\langle v_{g1}\rangle\rangle$ $\phi_{EXP}^{(2)} = \frac{2\langle a_{i2}\rangle}{3\langle\alpha_2\rangle}\frac{\partial}{\partial z}\langle\alpha_2\rangle\langle\langle v_{g2}\rangle\rangle$	Bubble Expansion
BT	$\phi_{BT}^{(1)} = -C\left(D_{c1}^*\right)^2\frac{\langle a_{i1}\rangle}{\langle\alpha_1\rangle}\frac{\partial}{\partial z}\langle\alpha_1\rangle\langle\langle v_{g1}\rangle\rangle$	Inter-group Transfer Due to Bubble Expansion

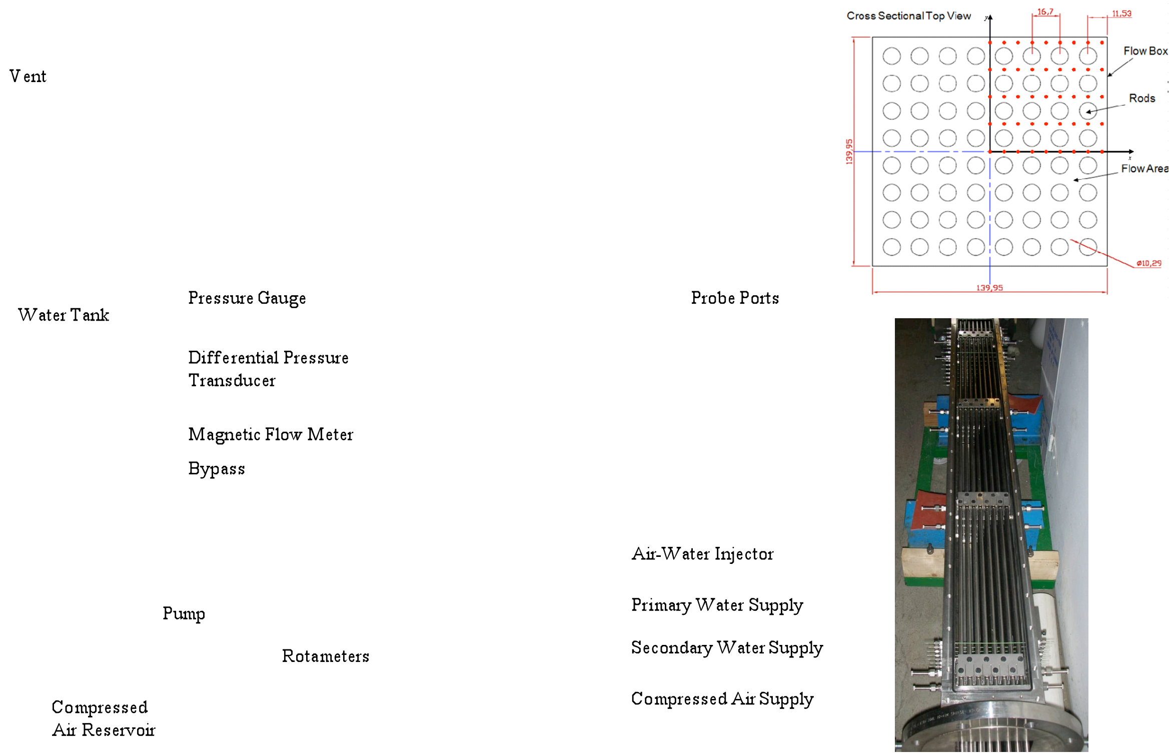

Figure 2 Test Section Schematic

Each measurement location allows measurement of local parameters at several locations in one-fourth of the test section. Using flow symmetry, it can be reasonably assumed that these profiles will be similar to those in the remainder of the test section. Local parameters are measured using four-sensor conductivity probes, while pressure drop is measured using pressure transducers. The four-sensor probes can be moved back and forth in the test section to measure several locations. These locations provide a map of the flow parameters in the subchannel and rod gap centers over one fourth of the test section. Details regarding the development and use of the four-sensor conductivity probe can be found in the literature [3]. Data was collected with acquisition rates of 35 kHz for a period of 120 seconds. Based on flow conditions present in this study, the uncertainty in the interfacial area concentration measurement is expected to be about ±15%.

The test conditions used in this experiment are shown in Fig. 3. The black lines in the figure represent the flow regime transitions predicted by Mishima and Ishii [3] for round pipes, while the colored lines represent the flow regime transitions based on flow regime identification in rod bundles performed using a neural network classification system. Tests were performed under absolute pressures of 100 kPa and 300 kPa, with void fractions ranging up to 0.77.

4. Results and Discussion

The experiments performed for this study resulted in a great deal of data. Twenty flow conditions were tested at 100 kPa system pressure, and another 17 conditions were tested at

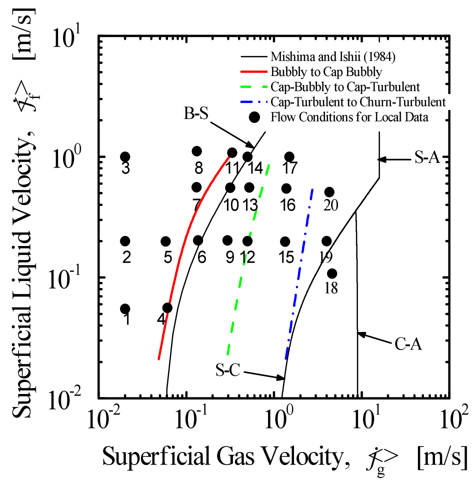

Figure 3 Test Conditions for Interfacial Area Concentration Measurements

300 kPa system pressure for a total of 37 flow conditions. These flow conditions covered flow regimes from bubbly flow to cap-bubbly flow and churn-turbulent flow. For each flow condition, measurements were performed at four axial locations and 45 local measurements were performed for each axial location, resulting in 6,660 local data points and 148 area-averaged measurements.

Figure 4 shows the typical flow patterns seen in preliminary tests in a transparent acrylic rod bundle with similar dimensions to the facility used in the current experiment. The upper-left shows bubbly flow, characterized by small, dispersed bubbles. Cap-bubbly flow, on the upper-right side, shows some larger cap-shaped bubbles, but the flow is still relatively stable. Cap-turbulent flow, on the bottom-left of the figure, is characterized by the presence of relatively stable cap-shaped bubbles with additional turbulent behavior. Churn turbulent flow, the last of the images, is characterized by large turbulent bubbles without a defined shape.

To illustrate the change in the characteristic length scale for different flow regimes, some representative centerline profiles are shown in Figs. 5 and 6 for bubbly and cap-turbulent flows, respectively. In the figures, the void fraction profile is shown in the upper-left, while the interfacial area concentration profile is shown in the upper-right, gas velocity in the lower-left and Sauter mean diameter in the lower-right. The data is differentiated by bubble size group and by subchannel center and rod gap measurements.

Figure 5 shows a distinct peak in void fraction in the gaps between rods compared to the subchannel center. This indicates a wall-peaked void profile, induced by the lift force. The lift force is dependent on the velocity gradient, which is highest in the rod gap center due to the proximity of the simulated fuel rods [4]. The peak gas velocity, however, does not show much difference between the rod gap and subchannel center even though the velocity near the rods should be very close to zero. This is because the measurement is taken in the center of the rod gap, where the actual velocity shows a peak and may not be much different than that in the subchannel center. Further, the relatively constant Sauter mean diameter shows that the bubble size distribution is not affected very strongly by the local geometry and leads to an

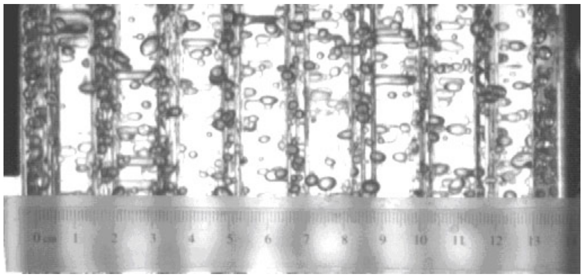

(a) bubbly flow

$\langle j_g \rangle$ = 0.02 m/s, $\langle j_f \rangle$ = 0.20 m/s.

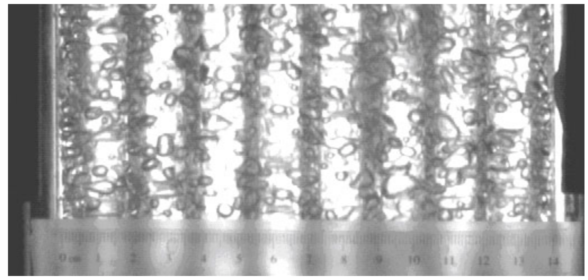

(b) cap bubbly flow

$\langle j_g \rangle$ = 0.14 m/s, $\langle j_f \rangle$ = 0.20 m/s.

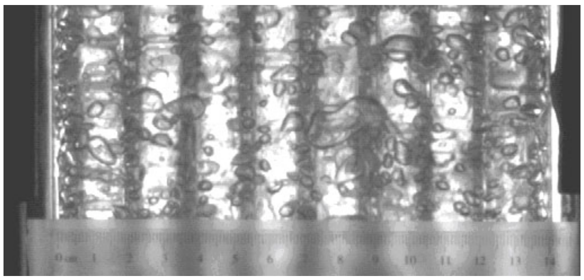

(c) Cap turbulent flow

$\langle j_g \rangle$ = 0.80 m/s, $\langle j_f \rangle$ = 0.21 m/s.

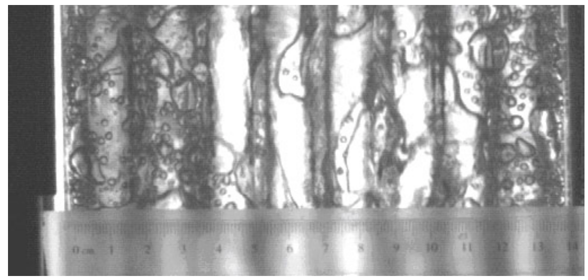

(d) Churn turbulent flow

$\langle j_g \rangle$ = 8.80 m/s, $\langle j_f \rangle$ = 0.20 m/s.

Figure 4 Flow visualization in various flow regimes

interfacial area concentration profile very similar to the void fraction profile. The data shows that the characteristic length scale is the subchannel hydraulic diameter for bubbly flows, and that similar subchannel distribution patterns with limited variation between subchannels are repeated throughout the bundle.

Figure 6 shows that the flow behavior changes significantly after Group 2 bubbles begin to form. Group 2 bubbles can grow to be larger than the subchannel size and therefore can span multiple subchannels. This has a multitude of effects on the flow, largely resulting in a shift in the dominant length scale from the subchannel hydraulic diameter to the casing hydraulic diameter. This leads to the effect shown in the figure, where the profile across the test section is much more significant than the profiles within each subchannel and the subchannel profile effects are largely eliminated. The local data then begins to look very similar to profiles expected in large diameter pipes or other large geometries. Also, it can be noted that there is very little difference in the Group 1 and 2 gas velocities. Although small bubbles tend to have smaller relative velocities than large bubbles, the presence of Group 2 bubbles results in wake entrainment, which can lead to higher liquid velocities behind the large bubble and can give the results shown in this figure, which indicate that the small Group1 bubbles can actually move faster than the larger Group 2 bubbles. The Sauter mean diameter for Group 1 is fairly constant across the test section and is very similar for both cases, indicating that the size distribution of Group 1 bubbles is not very sensitive to the local geometry. For Group 2, the effect of the fuel rods on the Sauter mean diameter is small.

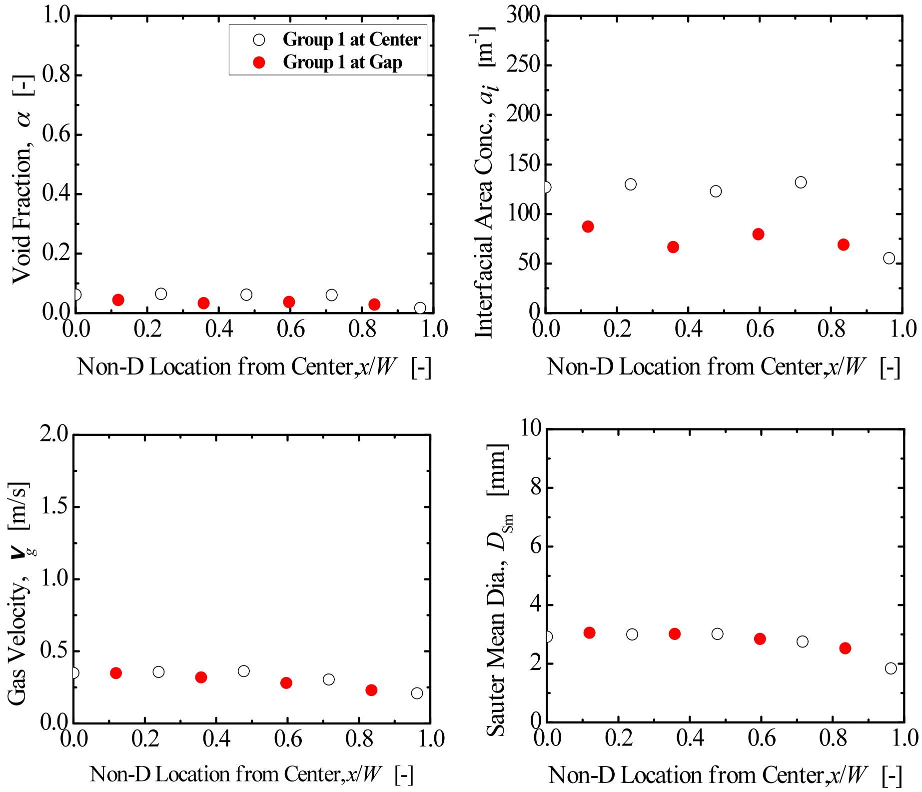

Figure 5 Bubbly flow centerline profile data with $\langle j_f \rangle$ = 0.07 m/s, $\langle j_g \rangle$ = 0.015 m/s

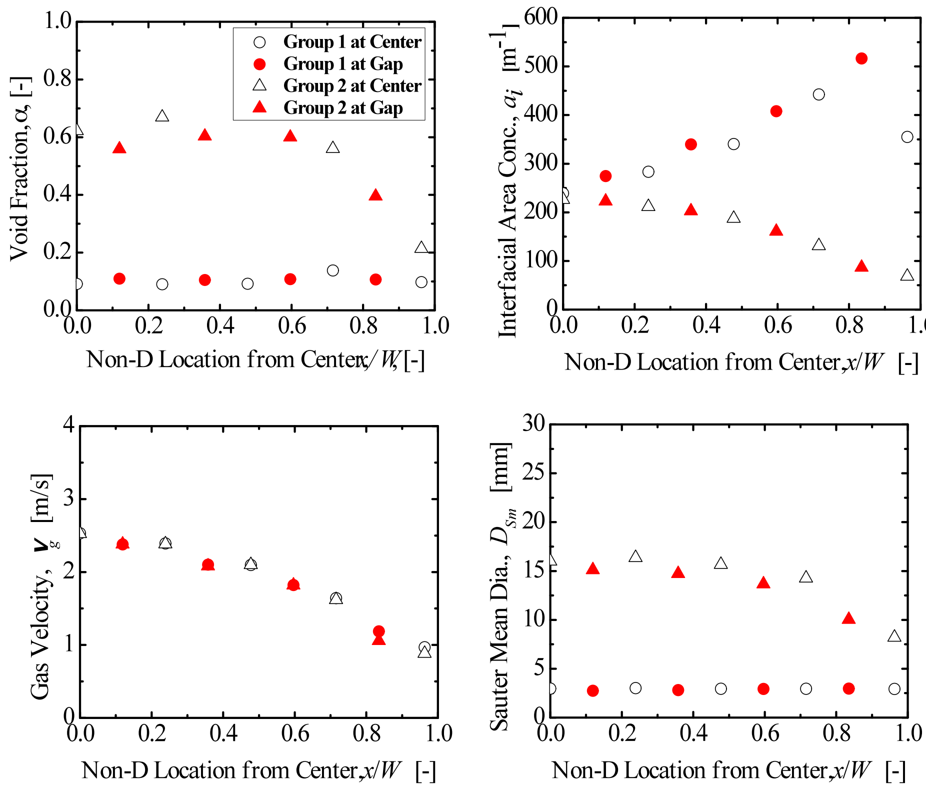

Figure 6 Cap turbulent flow centerline profile data with $\langle j_f \rangle$ = 0.59 m/s, $\langle j_g \rangle$ = 1.2 m/s

In order to evaluate the one-dimensional IATE models, the area-averaged void fraction and interfacial area concentrations are estimated from the local data though sophisticated interpolation scheme [5]. This scheme has been validated by comparing with one-dimensional void fraction and superficial gas velocity measurements. Figures 7 and 8 show the area-averaged void fraction, interfacial area concentration and gas velocity data along the axial direction for the same flow conditions noted in Figs. 5 and 6, with the locations of the grid spacers noted as dashed blue lines, Group 1 values as open circles, and Group 2 values as closed circles. This allows evaluation of the effect of grid spacers, which has been seen to be very complex, resulting in either coalescence or breakup of bubbles depending on the flow condition and system pressure.

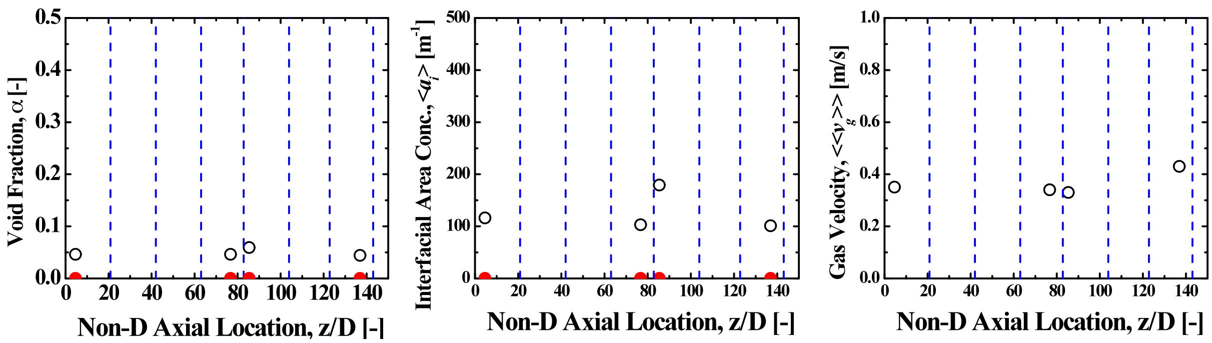

Figure 7 Area-averaged data for $<j_f>$ = 0.07 m/s, $<j_g>$ = 0.015 m/s

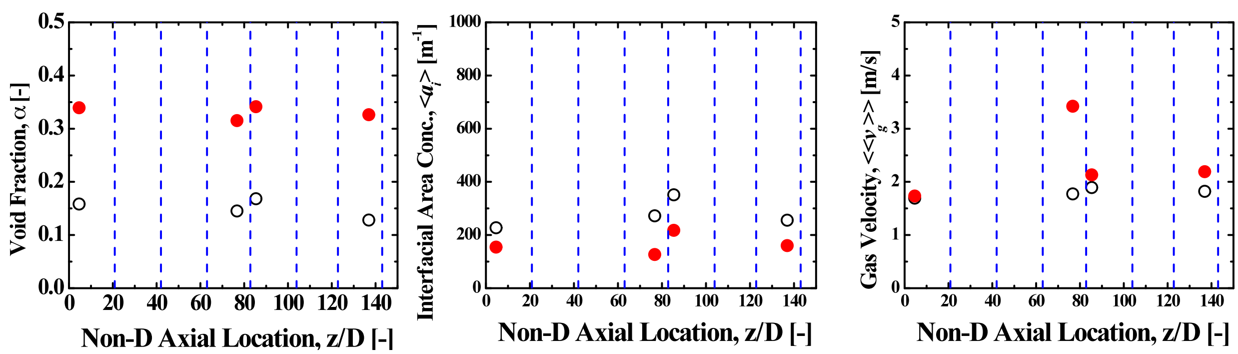

Figure 8 Area-averaged data for $<j_f>$ = 0.59 m/s, $<j_g>$ = 1.2 m/s

Since the measurement at z/D = 85 is immediately above a spacer, it is expected that a sudden change in the local parameters may occur. This will have a strong effect on the interfacial area concentration depending on the flow condition; however this is a very complex phenomenon that requires additional study and modelling effort. For this reason, this measurement location is ignored in the IATE evaluation because the interest in this study is on the average behavior of the flow.

To evaluate the performance of the IATE, the models described in Table 1 were included in a computer program to numerically solve the IATE with the test conditions and area-averaged data at the lowest measurement location as input. All of the models and coefficients used were the same as those given in Ishii and Hibiki [3] and determined using previous experimental data, with the exception of the gap size G, which was modified as described above. Figures 9 and 10 show the results of the IATE calculations and compare those results with the experimental data. The error bars in the figures represent errors of 30% between the prediction and measurement. Figure 9 shows a bubbly flow, or essentially one-group, calculation while Fig. 10 shows a flow condition in churn-turbulent flow, which requires both bubble groups. In each figure, the axial development of the interfacial area concentration and void fraction for both groups is shown along the left side, while the change in interfacial area concentration due to various mechanisms is shown for group 1 and group 2 along the right side. For bubbly flow, Fig. 9 shows the expected behavior. No Group 2 bubbles are predicted to exist, and the interfacial area concentration is quite well predicted. The dominant mechanisms are bubble growth due to expansion and wake entrainment between two Group 1 bubbles.

Figure 10, for cap-turbulent flow, also shows the expected trends. The void fraction development agrees very well with the data, and the interfacial area concentration prediction is also reasonable. For Group 1, the dominant source of interfacial area concentration is bubble expansion, while dominant sinks are wake entrainment by Group 2 bubbles and, to a lesser extent, coalescence due to random collision. For Group 2 the dominant sources are bubble expansion and wake entrainment of Group 1 bubbles, with coalescence of Group 1 bubbles by random collision having a small effect. Dominant sinks for Group 2 include random collision of Group 2 bubbles and wake entrainment of Group 2 bubbles.

Figure 11 show the comparison between the predicted and measured IAC at port z/D = 77 and z/D =137 at 300 kPa pressure condition. The dashed lines represent errors of ±30%. The overall performance of the IATE with the current source and sink models was evaluated by comparing the area-averaged data at each measurement location with the prediction developed by the model at z/D = 77 and 137, thereby comparing the predicted and actual change in interfacial area concentration. Overall the agreement between the data and model is quite good, especially for bubbly flows, with the data being predicted to within ±15%. At higher void fractions where Group 2 bubbles exist the data is predicted to within ±20%. Some outliers do exist, and this may be caused by the effect of the spacer grids under certain flow conditions. This indicates that the models perform reasonably well, however the accuracy of the models for Group 2 may be improved by specifying independent length scales for the two bubble groups. The gap size model used may impose too great a restriction on the size of Group 2 bubbles leading to over-prediction of interfacial area concentration. A more flexible model allowing the Group 1 and Group 2 length scales to be independently specified should improve the prediction accuracy for flows where both bubble groups are present. The development of a model for the effect of the spacer grid on the interfacial area concentration and void fraction distribution between the two groups would further improve the ability of the IATE to predict interfacial area concentration in two-phase flows.

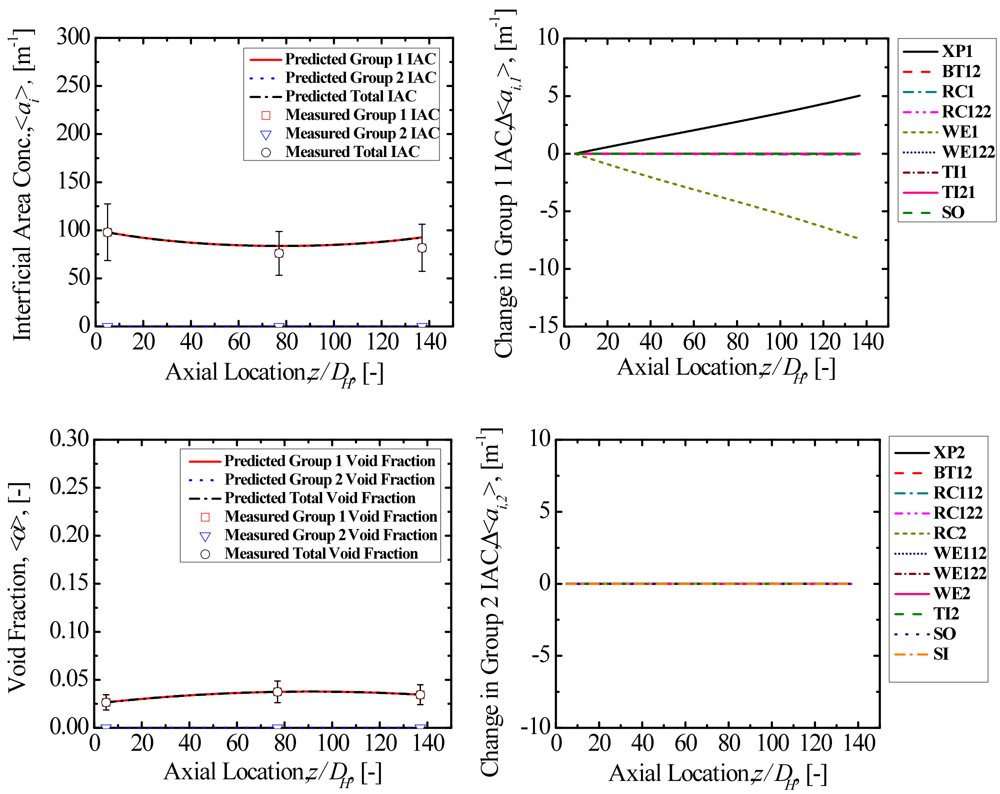

Figure 9 Axial Development at 300 kPa, $<j_f>$=0.07 m/s, $<j_g>$=0.015 m/s

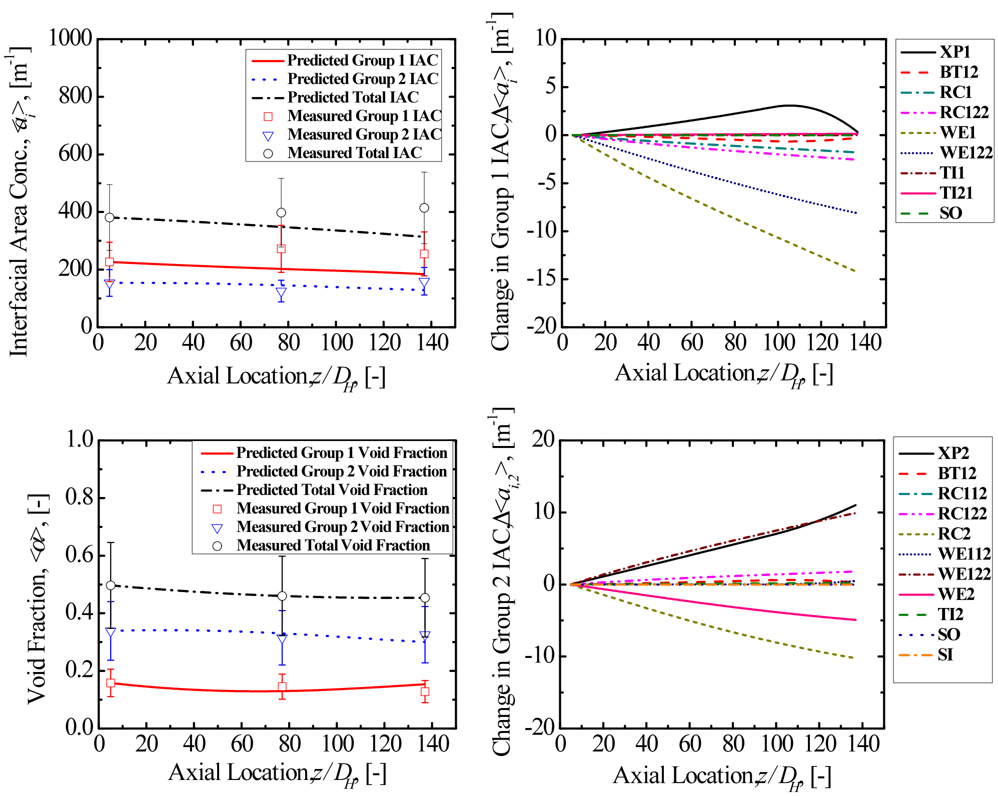

Figure 10 Axial Development at 300 kPa, $<j_f>$=0.59 m/s, $<j_g>$=1.2 m/s

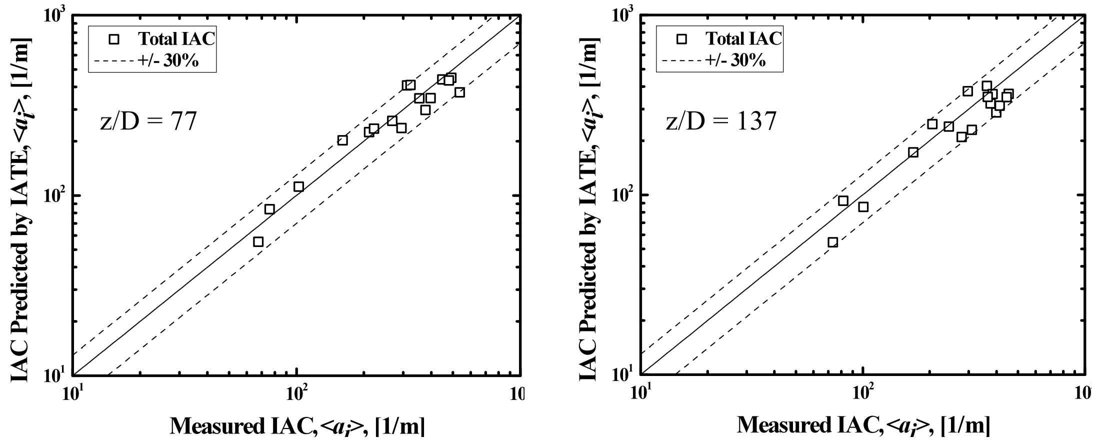

Figure 11 Interfacial Area Concentration Prediction Error for 300 kPa Pressure Condition

5. Conclusions

Experiments have been performed under 100 kPa and 300 kPa pressure conditions to measure the void fraction, interfacial area concentration, and bubble velocity. The liquid superficial velocities ranged from 0.06 m/s to 1.11 m/s, while the gas superficial velocities ranged from 0.02 m/s to 4.08 m/s. This resulted in void fractions ranging from 0.02 to 0.77. The results of simulations agree well with the data, the average relative error is generally within ±20% for IAC and void fraction. It was found that the current IATE performs well in bubbly flow and cap bubbly flow regime. Also, it was determined that the spacer grid has a significant effect on the interfacial area transport and that developing a model to predict this effect may significantly improve the performance of the IATE for rod bundle geometries.

6. Acknowledgement

This work was performed at Purdue University, in the Institute of Thermal Hydraulics, under the auspices of the U.S. Nuclear Regulatory Commission.

7. References

[1] T. Hibiki, M. Ishii, "Interfacial Area Transport Equations for Gas-Liquid Flow," *The Journal of Computational Multiphase Flows*, Vol. 1, 2009, pp. 1-22.
[2] S. Paranjape, M. Ishii, T. Hibiki, "Modeling and Measurement of Interfacial Area Concentration in Two-Phase Flow," *Nuclear Engineering and Design*, Vol. 240, 2010, pp. 2329-2337.
[3] M. Ishii and T. Hibiki, Thermo-Fluid Dynamics of Two-Phase Flow, Second Edition, Springer US, New York, 2010.
[4] T. Hibiki and M. Ishii, "Lift force in bubbly flow systems," *Chemical Engineering Science*, Vol. 62, 2007, pp. 6457-6474.
[5] M. Ishii, T. Hibiki, S. Paranjape, Y. Liu, X. Yang, and J.P. Schlegel. "Subtask 4: Interfacial Area Transport in a Rod Bundle," PU/NE-10-18, 2010.